Interconnectivity Explains High Canalicular Network Robustness between Neighboring Osteocyte Lacunae in Human Bone

Emely Bortel, Liam M Grover, Neil Eisenstein, Christian Seim, Heikki Suhonen, Alexandra Pacureanu, Peter Westenberger, Kay Raum, Max Langer, Francoise Peyrin, Owen Addison,* and Bernhard Hesse*

Osteocytes are the most frequent bone cells connected with each other through cell processes within tiny tubular-shaped canaliculi. The so-called osteocyte lacunar-canalicular network (LCN) plays a crucial role in bone remodeling and mineral homeostasis. Given the critical nature of these functions, it is herein hypothesized that the LCN must be structurally "overengineered" to provide network resilience. This hypothesis is tested by characterizing canalicular networks in human bone at the fundamental "building-block" level of LCN formed by two adjacent osteocytes. As the hierarchical micro- and macroscale structure of bone is influenced by anatomical location, subjected loads, and growth rate, three distinct tissue types are studied. These include femur, jaw, and heterotopic ossification (HO), a rapidly forming mineralized tissue found in soft tissue compartments following severe trauma. It is found that the LCNs at the fundamental level are composed of hundreds of canalicular segments but of only few separated groups of linked canaliculi (canalicular clusters), resulting in a strongly pronounced interconnectivity. Fluid permeability simulations on intact and artificially altered LCN suggest that the function of the LCN is not only to optimize rapid and efficient access to bone mineral, but also to maintain high permeability when inevitable local interruption of canaliculi occurs.

1. Introduction

Human bone is a highly dynamic tissue, hierarchically structured at multiple levels. It provides the body mechanical support, protects inner organs, and acts as a reservoir for mineral homeostasis.[1] Bone remodels continuously throughout life, under the control of bone-forming (osteoblasts) and mineral-resorbing (osteoclast) cells. However, the most common cells within bone are osteocytes, found with a density of 10 000–40 000 per mm^3.[2–5] Adjacent osteocytes are intimately associated with each other, forming a complex housed in fluid-filled interconnected spaces within bone, known as the lacunar-canalicular network (LCN). The LCN plays an important role in both the regulation of bone mass and bone remodeling, but its structure–functional relationship remains only partially understood. Recent advances in submicron resolution 3D imaging of bone have provided new insight, especially into the variability in size, shape, and distribution of osteocyte lacunae and their associated canaliculi that contain the cells' radially projecting, long dendritic processes.[6] The number of canaliculi that are connected to individual lacunae, described as primary canaliculi, is now known to vary considerably, ranging from ≈40 to 120.[7–10] Branching of the canaliculi at various distances from the lacunae further increases the density of the network within the mineralized matrix.[11–15] However, the significance of these branching remains uncertain and the number of individual canalicular clusters that connect different lacunae, hypothesized to represent the level of redundancy in the interconnectivity of the LCN, is not known.

E. Bortel, C. Seim, B. Hesse
Xploraytion GmbH
Bismarckstrasse 10-12, 10625 Berlin, Germany
E-mail: hesse@xploraytion.com

L. M. Grover, N. Eisenstein
School of Chemical Engineering
University of Birmingham
B15 2TT Birmingham, UK

C. Seim
Technical University of Berlin: Institute of Optics and Atomic Physics
10623 Berlin, Germany

H. Suhonen
University of Helsinki: Department of Physics
00560 Helsinki, Finland

A. Pacureanu, F. Peyrin, B. Hesse
ESRF: Experiment Division
38000 Grenoble, France

ADVANCED
SCIENCE NEWS
www.advancedsciencenews.com

ADVANCED
NanoBiomed
RESEARCH
Open Access

www.advnanobiomedres.com

Previously, confocal scanning microscopy was already proven to be able to image large fields of view of the bone LCN and to quantify the network topology[16] and was further exploited for simulating fluid flow inside the LCN.[17–19] Fluid flow inside the LCN is thought to be the fundamental mechanism for mechanosensation by osteocytes.[11,20] The morphology and connectivity of the LCN influence the fluid flow inside the LCN and therefore significantly impact cellular physiology.[21–23] Recently, Wittig et al. reported on the presence of different canalicular junctions in the bone of various vertebrate species and estimated using numerical models their impact on fluid-induced pressure inside the LCN concluding a critical role of the presence of junctions on liquid mass transport and flow velocities and used synchrotron nanoCT for the imaging of their samples.[15] Beyond mechanosensation,[14] fluid flow in the LCN has been shown to also be central to achieving mineral homeostasis.[16] Due to the incredibly high spatial density of the LCN, it has been estimated that 80% of the mineralized tissue in humans is located within 2.8 μm of the closest LCN boundary and 50% within 1.5 μm.[11,24,25] The proposed significance of this intimate relationship and the capacity and relevance for mineral exchange has recently been discussed in detail by Qing and Bonewald.[26]

Quantitative high-resolution 3D imaging and volumetric data analysis methods have become important tools in understanding the structure–function relationships between canaliculi (typically <1 μm in diameter) and adjacent mineralized matrix. Roschger et al. identified a positive correlation between the LCN and mineral densities,[13] supporting earlier findings from synchrotron X-ray nanoCT data which quantified pericanalicular mass densities at different tissue mineralization stages, hypothesizing that mineral exchange occurs at all LCN boundaries.[24] Imaging data have also informed modeling of the LCN structure using complex network analysis theory.[27] Investigating both murine and ovine bone it was concluded that the LCN is integral to functions of intercellular transport and communication. While the study reported differences in LCN functionality between slow- and fast-growing bones, the study reported no statistical differences in topological properties. The authors suggested that at the subcellular level, the LCN showed conserved functional similarities between species and then linked their findings to the efficiency of the LCN in distributing material and information. They concluded that the function of the osteocyte network was "to access as much bone as possible with as few cells as possible."[27] An intact LCN is therefore considered essential to maintain sufficient fluid-flow, mechanical transduction and communication

between the cells enabling bone remodeling and repair to be orchestrated. Conversely, interruptions of the LCN due to micro-crack formation[28–31] occlusion with mineral,[32–35] or a decrease of the canalicular density with age[36–38] may compromise the LCNs' functional ability to control mineral homeostasis and maintain tissue health.

Given the critical nature of these functions, we hypothesize that the LCN must be structurally "overengineered" to provide network resilience. Here, we test this hypothesis by characterizing canalicular networks in human bone at the fundamental "building-block" level of two adjacent osteocytes. As the hierarchical micro- and macroscale structure of bone is significantly influenced by anatomical location, subjected loads, and growth rate, three distinct tissue types were studies. These included cortical bone from jaw and femur as well as heterotopic ossification (HO), a rapidly forming mineralized tissue found in soft tissue compartments following severe trauma, spinal cord injury, or neuronal disorders.[39] As HO develops in such short time scales and has no load bearing function, it provides a unique subject for to study LCN structure. To investigate whether interruption of the integrity of individual canaliculi affects the functional performance of the LCN, we first segmented the LCN of connected osteocyte lacunae before characterizing the interconnectivity between individual canaliculi. Subsequently, the impact of disruption to neighboring cells LCN was studied in terms of fluid permeability and mineral access using single-phase fluid flow simulations on the intact and on a simulated damaged LCN.

2. Results

The LCN of two neighboring lacunae, randomly selected for analysis from each volume studied, was segmented for two different regions each in femoral, mandibular, and three regions of HO tissue from seven different donors (**Figure 1**).

2.1. Different Types of Canaliculi Intersections

Irrespective of tissue type, the segmented canaliculi networks connecting two individual lacunae demonstrated different types of junctions and branching, which are shown schematically in **Figure 2**. The simplest case of a straight connection (A) between lacunae without branching was observed only relatively sparingly. Most commonly, types B and C (simple branching and junctions close to a lacuna) were found (see **Table 1**). Large junctions, where more than four canaliculi intersect (E), were
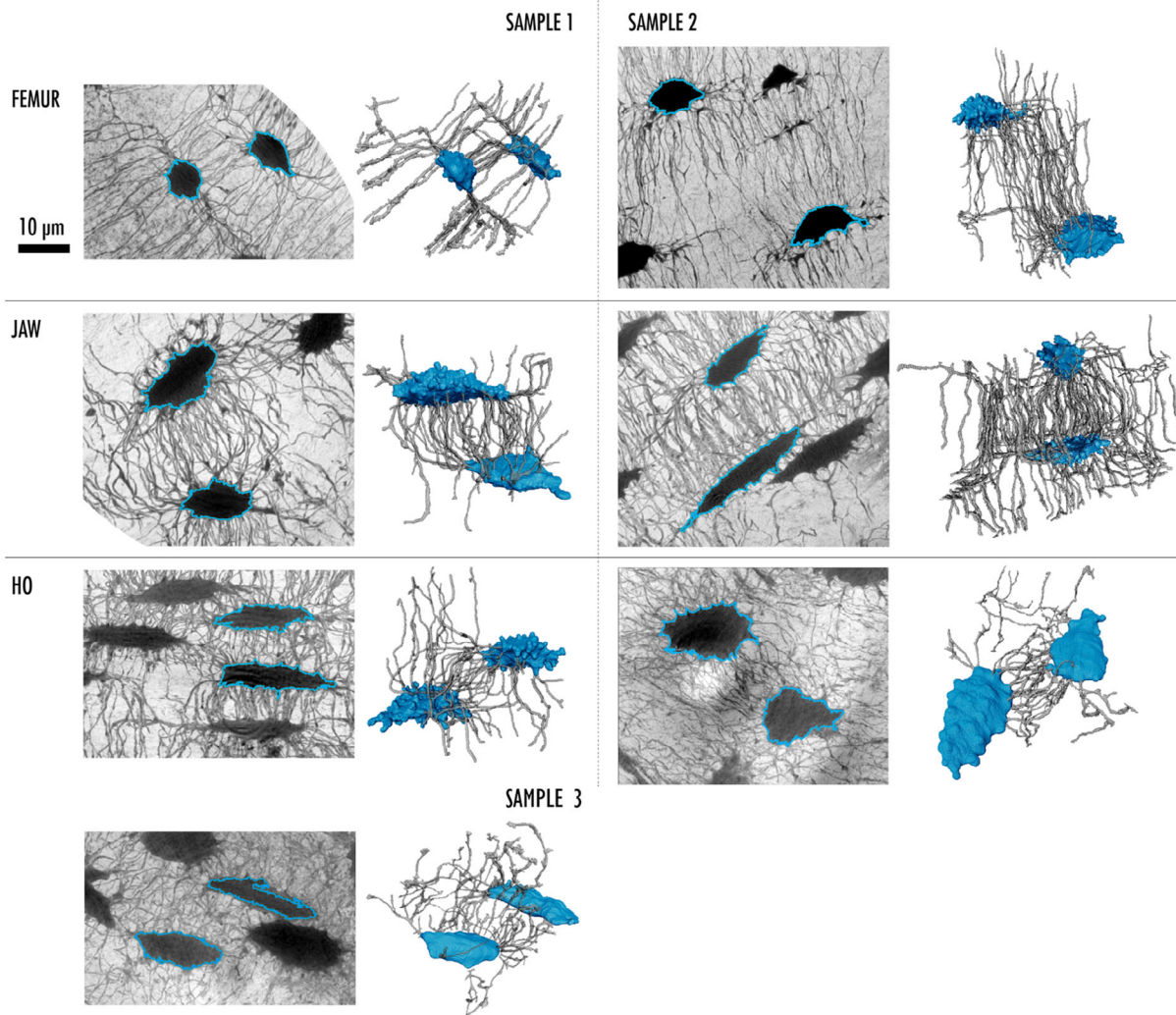
P. Westenberger
Thermo Fisher Scientific
40239 Düsseldorf, Germany

K. Raum
Charité—Universitätsmedizin Berlin
Corporate Member of Freie Universität Berlin
Humboldt-Universität zu Berlin, and Berlin Institute of Health
BCRT—Berlin Institute of Health Center for Regenerative Therapies
13353 Berlin, Germany

M. Langer, F. Peyrin
Univ Lyon
CNRS 5220, Inserm U1294, INSA Lyon
69621 Creatis, Villeurbanne Cedex, France

O. Addison
Faculty of Dentistry
Oral and Craniofacial Sciences
Kings College
SE1 9RT London, UK
E-mail: owen.addison@kcl.ac.uk

M. Langer
Université Grenoble Alpes
CNRS, UMR 5525
VetAgro Sup, Grenoble INP, TIMC
F-38000 Grenoble, France

ADVANCED
SCIENCE NEWS
www.advancedsciencenews.com

ADVANCED
NANOBIOMED
RESEARCH
Open Access
www.advnanobiomedres.com

Figure 1. Minimum intensity projections (MIPs) and volume renderings of the LCN of the seven different tissue regions analyzed within this study. The blue outlined cells indicate those that are selected for further analysis shown in the renderings next to each MIP. All images have the same scale bar.
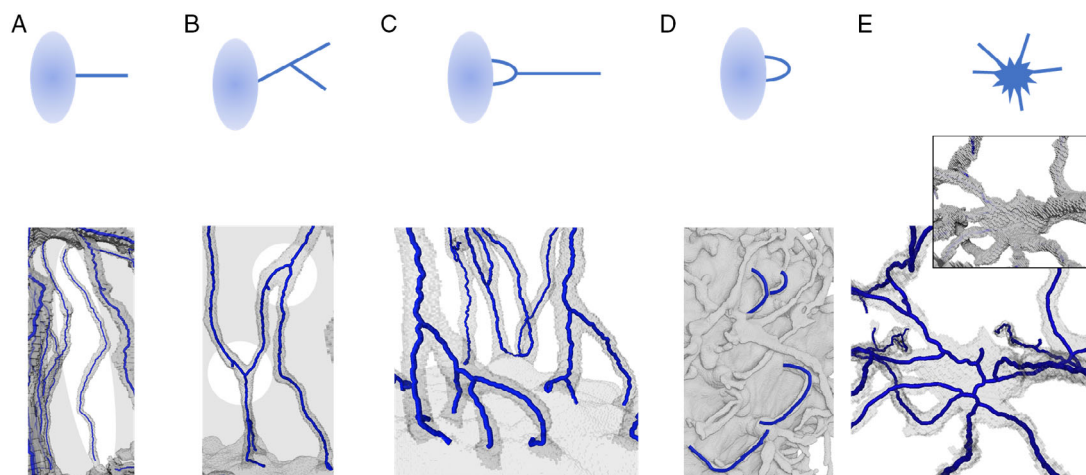
observed in all except one sample (Table 1), albeit with only a few occurrences. In some networks, especially when lacunae were close to a cement line or to a microcrack, we found canaliculi that exit a lacuna and then reconnect back to the same lacuna (see also Figure S1, Supporting Information). These types have been observed and are mentioned here for the sake of completeness. However, as they are part of only one of the two lacunae, they are not further analyzed within the connected component analysis, as the criterion was that the canaliculi must be connected to the two considered lacunae.

2.2. Morphology of the Canalicular Network

The segmented LCNs contained between 3 and 13 individual canaliculi clusters (Table 1). As segmentation is a crucial and nontrivial part of the analysis of these small structures, and because the choice of the volumes of interest (VOIs) may crop some connecting canaliculi, we assume that the degree of

interconnectivity between these clusters may even be higher, resulting in less individual clusters. The number of canaliculi exiting the lacunae was similar for both connected lacunae of each pair of neighboring lacunae, except for one case—sample jaw 1 (see **Table 2**), where more than twice as many canaliculi exited lacuna 2. These, however, include a lot of y-shaped connections close the lacuna. Overall, it seems that there is a tendency of fewer canaliculi exiting the lacunae in the HO sample. The canalicular volume porosity (Ca.V/BV) ranged between $\approx$0.5% and 2.1%, with the lower values occurring in the HO samples. The canalicular surface density (Ca.S/BV) ranged between 0.06 and 0.17 μm^{-1}; the canalicular surface densities of all three HO samples were smaller than the densities of all the other four samples. The distance to the canalicular interfaces in which 50% of the mineral volume is located in was found to be between 1.5 and 2.1 μm. The level of alignment (LoA) varied between 0.006 and 0.024 (see Figure S2, Supporting Information). Again, all HO samples have slightly lower values

www.advancedsciencenews.com

ADVANCED
NANOBIOMED
RESEARCH
Open Access

www.advnanobiomedres.com

Figure 2. Generic types of intersections between canaliculi that were observed in the segmented data: A) individual canaliculi between 2 lacunae, B) branching, (C) γ-shaped connections, D) branching back to the same lacuna, and E) canaliculi junctions connecting more than four canaliculi. To assess the scaling note that the canalicular diameter is about 0.5 μm.

(not significantly though) than the compact bone. The canalicular length per bone volume ranged from 0.04 to 0.07 μm μm^{-3}, with its mean at 0.06 μm μm^{-3} (0.06 μm μm^{-3} is the equivalent of 60 km of canalicular length per cm^3). The number of nodes varied widely from less than 50 nodes in femur 1 to as high as ≈300 for jaw 2. However, the number of nodes scaled linearly with the total canalicular length (Figure S3, Supporting Information), Therefore the average canalicular segment length does not differ greatly between samples (6.5 ± 1.6 μm). Some of the parameters are graphically shown Figure S4, Supporting Information.

2.3. Fluid Transport within the LCN

The impact of the interconnections on the fluid transport capacity and on the material accessibility after simulated interruption of an individual segment is shown schematically in **Figure 3**. It can be seen that although interconnections come at the cost of increased total canalicular network length, they act to stabilize the overall network performance. If an interruption of one segment occurs, a larger mineralized material volume always remains accessible in the interconnected system. In the given example, a blockage of one segment leads to a loss of 50% of all canals and 50% of the volume is not accessible anymore in the parallel system. The high interconnectivity leads to a loss of only 20% of the canals and a maintenance of 75% of the volume. Permeability experiments on the segmented LCN of the bone data were performed to study the effect of interrupted canaliculi on the fluid permeability between two lacunae and on the internal fluid flow. The permeability simulations were performed within the intact LCN and with an artificially introduced simulated crack separating all but one of the canaliculi close to one of the lacunae (**Figure 4**). For the intact (Figure 4a) and interrupted (Figure 4b) case, the fluid velocities are represented by a heat map on the 3D rendered surface of the segmented data. As the canaliculi reveal different thicknesses and surface topology, the fluid velocities are different between different adjacent segments.

The virtually altered LCN shows drastically decreased velocities; however, the branching and interconnectivity leads to a bigger material volume that is still accessible as compared to a case of a LCN consisting of individual, nonbranched canaliculi. The calculated permeabilities are given in Table 2 and it can be seen that the intact case permeabilities are several times higher than the ones calculated in the interrupted cases (13–30 times higher). This might be directly related to the degree of interconnectivity and thus the "path" the fluid could flow to circumvent the interruption.

Additionally, fluid simulations were performed on the LCN containing only one cluster in an intact situation (Figure 4e) and with one interruption arbitrarily cutting one canaliculus (Figure 4f). The zoom-ins (Figure 4e′,f′) show that the fluid velocity in the neighboring canaliculi increases slightly with a cut (white arrow). This is even more pronounced in the heat map showing the fluid velocities within the canaliculi (Figure 4g′,g″). The permeability in the altered cluster reduced from 1.36×10^{-5} to 1.31×10^{-5} μm^2. In a nonbranched situation, one would expect a higher drop because permeability would be largely proportional to the number of canaliculi.

This is schematically also shown in **Figure 5**, where virtual cross sections through a clustered LCN (a)) and a schematic parallel system (b)) show that due to the high interconnectivity the fluid has multiply pathways to circumvent a possible disruption. In the other case, a complete connection from one lacuna to the other is lost.

These observations suggest that the high interconnectivity stabilizes the LCNs' functional integrity against interruptions because 1) more material volume is still accessible for rapid and efficient access to bone mineral and mechanosensation, and 2) higher permeability is maintained.

3. Discussion

Simulations of fluid flow and of the permeability of the LCN have previously been limited to simplified models[9,40] that fail to fully

Table 1. Morphology of the connected canaliculi and sample details. Calculated parameters include the number of clusters ($Ca_{Clust}.N$), the number of connections to the lacunae 1 or 2 ($Ca.N_{LC}$), the volume the canaliculi supply (BV.VOI), the canaliculi volumes and volume fractions (Ca.V, Ca.V/BV), and the canal surface fractions (Ca.SA/BV, Ca.SA/Ca.V). The table also provides the distance to the canalicular network in which 50% and 80% of the mineral is located ($Ca\text{-}Dist_{50}$ and $Ca.Dist_{80}$)), the LoA, the total length of all canaliculi (Ca.L) extracted from the skeleton, the average canaliculi thickness (Ca.Th), and the average length of a segment between two nodes ($Ca.L_{Seg}$) and the counted junctions in the network. Each junction has been analyzed according to the number of segments attached to it (three segments: $Ca.Node_3$, four segments: $Ca.Node_4$, more than four: $Ca.Node_{Junction}$). Based on the different nodes, the mean number of segment per node is calculated (nodes/seg).

|		Femur 1[a]	Femur 2	Jaw 1[a]	Jaw 2	HO 1[a]	HO 2	HO 3	Mean	Stdev
		F, 70 years	F, 66 years	F, 70 years BRONJ, plasmacytoma	M, 19 years	M, 25 years blast injury	M, 42 years blast injury	M, 36 years high velocity impact		
$Ca_{clust}.N$		13	6	3	8	6	4	4	6.3	3.1
$Ca.N_{LC1}$		20	32	18	45	22	12	20	24.1	10.1
$Ca.N_{LC2}$		22	36	52	47	26	17	9	29.9	14.6
BV.VOI	$10^4 \mu m^3$	1.4	2.6	1.9	6.1	1.4	1.5	1.4	2.4	1.6
Ca.V	μm^3	287	274	413	1080	153	72	150	347.0	316.9
Ca.V/BV	%	2.0	1.0	2.1	1.8	1.1	0.5	1.0	1.4	0.6
Ca.SA	μm^2	2178	3080	3235	8687	1616	917	1452	3023	2442
Ca.SA/BV	$1/\mu m$	0.15	0.12	0.17	0.14	0.11	0.06	0.10	1.4	0.6
Ca.SA/Ca.V	$1/\mu m$	7.57	11.24	7.84	8.04	10.57	12.81	9.67	9.7	1.8
$Ca.Dist_{50}$	μm	1.6	1.5	1.5	1.7	1.6	2.1	1.5	1.6	0.2
$Ca.Dist_{80}$	μm	2.8	2.5	2.4	2.8	2.7	3.6	2.9	2.8	0.3
LoA		0.008	0.024	0.008	0.009	0.007	0.006	0.006	0.010	0.006
Ca.L	μm	825	1730	1420	3690	870	581	985	1443	985
Ca.L/BV	$\mu m/\mu m^3$	0.06	0.07	0.07	0.06	0.06	0.04	0.07	0.06	0.01
$Ca.Node_3$		38	96	69	244	105	47	56	93.6	65.5
$Ca.Node_4$		7	17	20	38	11	16	12	17.3	9.3
$Ca.Node_{Junctions}$		4	6	6	13	0	2	5	5.1	1.4
Nodes/BV	$1/1000\mu m^3$	3.5	4.5	4.9	4.8	8.2	4.4	5.1	5.1	1.4
Nodes/Ca.L	$1/\mu m$	0.06	0.07	0.07	0.08	0.13	0.11	0.07	0.08	0.03
Nodes/Seg		3.3	3.2	3.3	3.2	3.1	3.3	3.3	3.3	0.1
Ca.Th	μm	0.7	0.4	0.6	0.6	0.5	0.4	0.4	0.5	0.1
$Ca.L_{Seg}$	μm	8.1	7.6	7.3	7.1	4.3	4.8	7.3	6.6	1.4
N.Seg		102	227	194	521	204	122	135.0	214.8	132.0

[a]Indicates which sample was used for fluid simulations.

Table 2. Summary of the fluid flow simulations. Permeability and ratios for the intact case and when the LCN is virtually altered such that only one canaliculus remains connected to that lacuna where the virtual cut was located are shown. Crack 1 and crack 2 means that the virtually cut was made close to lacuna 1 and lacuna 2, respectively. the flow direction was from the cut side to the other lacuna.

Sample	Permeability						Ratio (intact/defect)	
	Intact		Crack 1		Crack 2			
	$k\ [\mu m^2]$	$k\ [d]$	$k\ [\mu m^2]$	$k\ [d]$	$k\ [\mu m^2]$	$k\ [d]$	Crack 1	Crack 2
Femur	8.74E-06	8.86E-06	2.86E-07	2.89E-07	6.70E-07	6.79E-07	30.56	13.04
Jaw	3.62E-05	3.66E-05	1.84E-06	1.87E-06	1.81E-06	1.81E-06	19.67	20.00
HO	6.36E-06	6.45E-06	3.62E-07	3.67E-07	4.51E-07	4.56E-07	17.57	14.10

represent the canaliculi structure and branching that has been addressed in this study through rigorous segmentation of nanoCT data. Canaliculi around a osteocyte lacuna play a crucial role in cell communication and transport mechanisms and their number has been estimated using various techniques such as confocal microscopy,[9] nanoCT,[7,8,41] and ptychography.[42] Here, we highlight the presence of intersections between canaliculi, detail the morphology of interconnections in the LCN
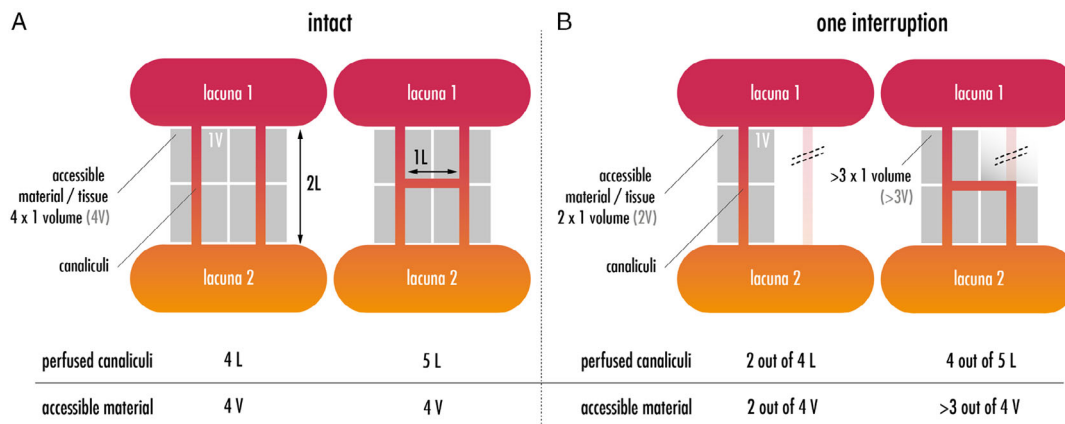
Figure 3. Schematic illustration of two lacunae connected via canaliculi. (A) The intact case, where two canaliculi connect two lacunae without (left) and with interconnections (right). For simplicity, the mineralized material accessible by the canaliculi is depicted as gray squares. B) One interruption hinders the fluid transport within certain canaliculi. In the case of interconnected canaliculi, only a shorter canal segment is lost and a larger volume remains accessible.

between two neighboring lacunae, and highlight their role in stabilizing bone mineral accessibility and fluid flow capacity. At this basic structural level, intersections of canaliculi from adjacent osteocytes were observed to result in few discrete canalicular clusters between neighboring lacunae (3–13) that appear to maintain the robustness of the network to perturbations. The robustness of the LCN is implemented at different length scales, with the network robustness between two cells as the most basic scale. Recently, other studies used confocal microscopy to assess the network properties on larger length scales and also report redundancies to increase network robustness.[18,19,27] Interruptions of individual canalicular segments lead to an altered flow pattern within the concerned canalicular cluster and could play a role in the osteocyte's capabilities to sense their extracellular space. In addition, the interconnections of the canaliculi also lead to different fluid velocities before and after branching of canaliculi and result in an amplified fluid velocities subsequently experienced by the osteocyte and thus contribute to previously reported flow-induced mechanotransduction.[43–45]

Recently, Wittig et al. showed the presence of canalicular junctions in various vertebrate species (including human bone) and highlighted their role in fluid transport within the LCN.[15] In this study, we confirm the existence of these junctions and additionally report on their frequency with respect to branching morphology (nodes that are formed by three or four canalicular segments). Branching is proposed to reduce the maximum pressure within the LCN,[23] and we speculate that the complex interconnectivity arising from the presence of nodes with more than three canalicular segments results in complex fluid flow patterns that have not been studied in computational fluid dynamics simulations to date. This high interconnectivity of the canalicular network leads to homogeneous and efficient access to mineral. Even after interruption of individual canaliculi or canalicular segments, the mineralized bone space is still widely accessible and in close distance to other canalicular segments still part of the fluid supplied network. Thus, the surface area of the supplied part of the LCN remains very high, indicating a high potential for mineral exchange at its surface. We report that the local

canalicular surface density ranges between about 0.06 and 0.17 $\mu m^2/\mu m^3$ and that 50% of the mineralized tissue is located within less than ≈1.6 μm from the closest canalicular surface. These numbers strongly support the assertion of the LCN having a crucial role and involvement in mineral homeostasis. Mineralized regions remain largely accessible by means of a short distance to nearest canalicular surface, even if individual canalicular segments are blocked or disrupted. This leads to these tissue regions being potentially more homogeneously mineralized when compared with regions with a more inhomogeneous canalicular density distribution. More homogeneous local tissue mineralization likely also impacts the stress or strain distribution in these regions toward potentially more homogeneous stress and strain fields.

The transport capabilities of the LCN was recently analyzed and quantified by Kollmannsberger et al. in ovine bone,[27] concluding that there are differences on the tissue level of the LCN in efficiency between different bone types. The LCN topology on the subcellular level is not distinguishable between different bone types; however, interestingly we observe a comparable overall morphology of the LCN in three very different anatomical human sites which are all exposed to very different mechanical load. Most interestingly, in the case of HO which should experience insignificant functional loading, descriptively the LCN does appear not totally different when compared to femur or jaw. We observe that the parameter ranges of HO samples are overlapping with those of jaw or femur for the clustering of canaliculi, number of canaliculi emitted by the lacunae, relative canalicular volume or surface area, distance of mineral to the canaliculi, canalicular length, number of nodes, and node density, canalicular thickness, and segment length. The total canalicular volume, the total canalicular surface, and the canalicular alignment of the three HO samples are smaller as compared to the other four samples. However, due to the small sample size no statistical testing was applied. For HO not only the mechanical load is very different to other bone sites but also the speed at which HO bone is formed. Future studies should refine further how the LCN of HO is different to the LCN of normally formed cortical bone. When
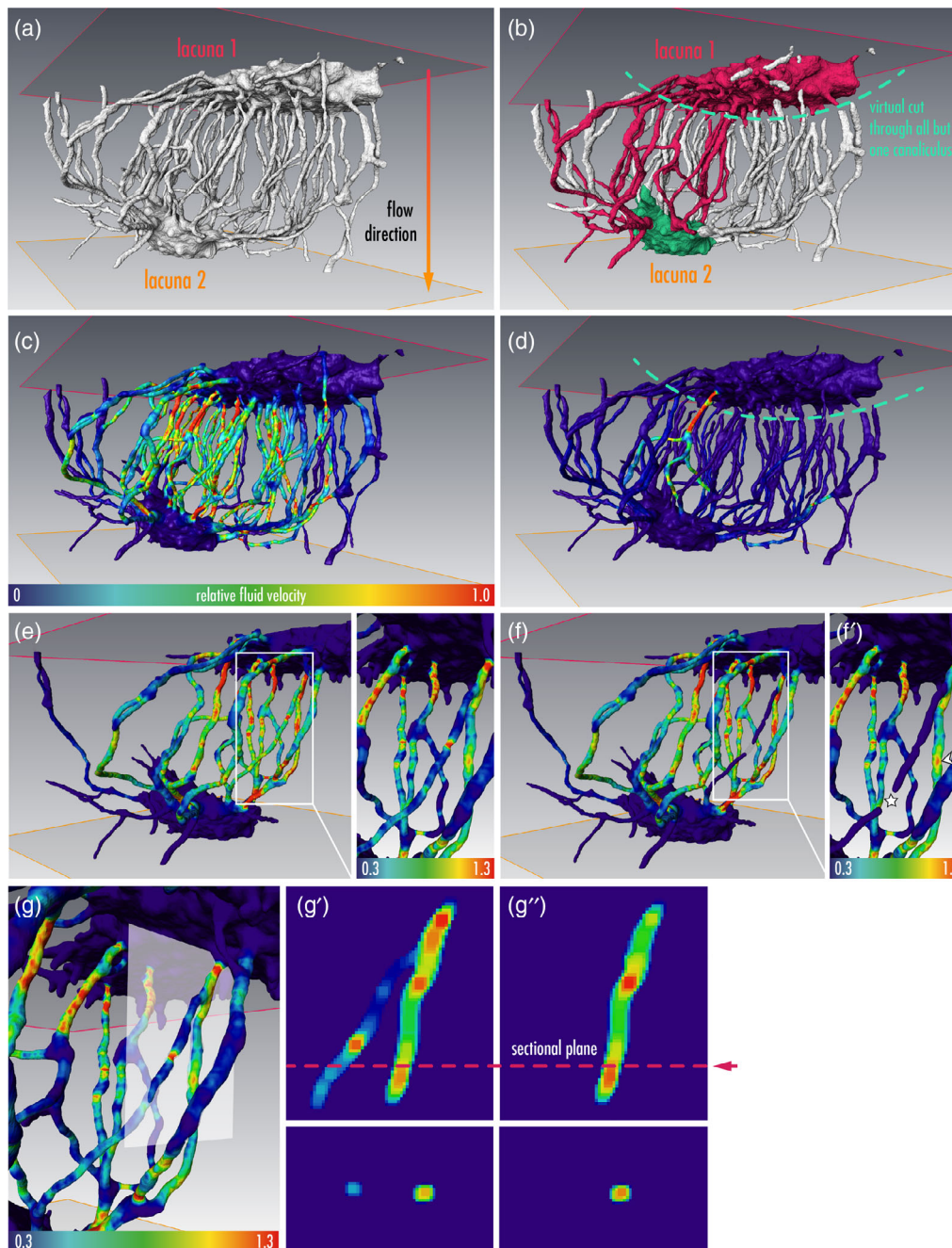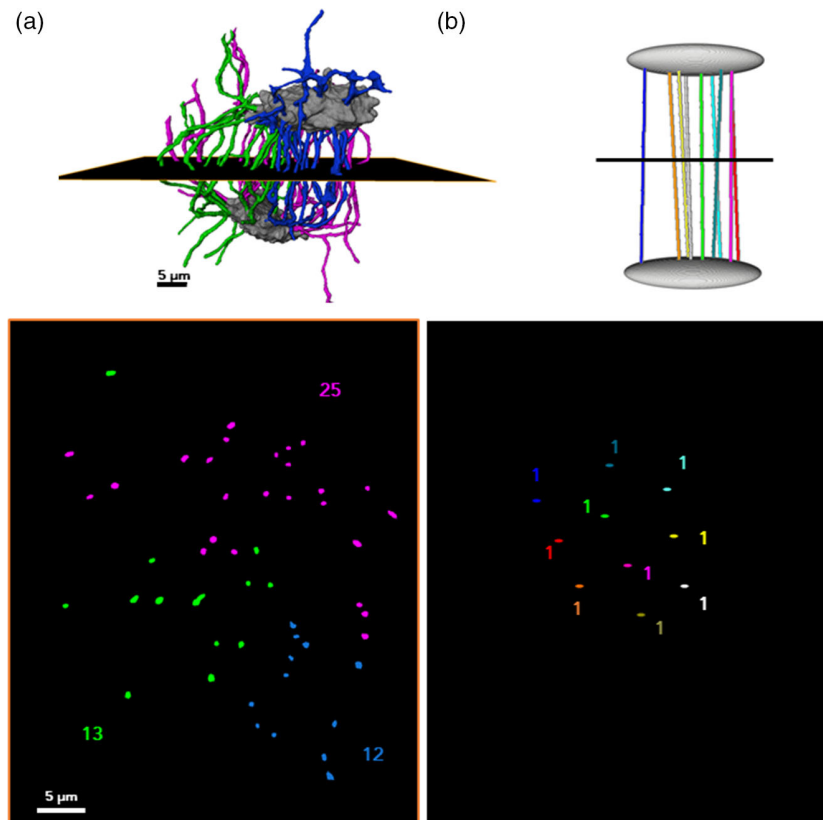
Figure 4. Representative fluid simulation experiment overview (jaw sample). In this example, the fluid flow simulation was performed from the top (pink) plane toward the bottom (orange) plane. a) An intact segmented LCN is shown. b) Virtual cuts/cracks disrupt all but one canaliculus close to lacuna 1. In addition, the canaliculi that are part of the cluster containing the one canaliculus that is not virtually cut from lacuna 1 are marked in pink. Fluid flow simulations were performed and the heat maps show the fluid velocities on the surfaces of the LCN in both c) intact and d) altered configuration. e,f) Only the pink cluster is used for fluid simulations for an intact (e) and one disrupted canaliculus version of the LCN (f). The subgraphs (g′) and (g″) show the fluid velocities within the intact and altered canaliculi.

comparing the LCN properties we observed the canalicular density to be (Ca.L/BV) $0.06 \pm 0.01\,\mu m\,\mu m^{-3}$ which is in line with a previous study in humans[46] and about half that of the values reported by Kollmannsberger et al. for woven (mouse) bone samples and about 3 times smaller than fibrolammellar bone (sheep). With respect to the number of segments connected to a node, we

found 3.25 ± 0.09 as an average value for the data of this study which is within the range and even very close to those given for ovine bone[27] (3.28 ± 0.01). The node density, however, was ≈ 10 times smaller for our data as compared to ovine bone.

Our data confirm that some morphological descriptors of the LCN (such as degree of nodes) are very similar between

**ADVANCED
SCIENCE NEWS**

www.advancedsciencenews.com

**ADVANCED
NANOBIOMED
RESEARCH**

www.advnanobiomedres.com

Figure 5. Cluster representation of an LCN in 3D in a 2D orthoslice. All canaliculi of one cluster have the same color. a) A highly interconnected LCN is shown, only consisting of three clusters, where each cluster has 12, 13, or 25 canaliculi in the shown plane. b) A purely parallel, not branched LCN. In the orthoslice, ten individual canaliculi are found.

anatomical sites even when compared to other vertebrate species. Nevertheless, other values such as canalicular density changed drastically from one subject to another and even more between species. For example, comparing our data (human bone) to ovine bone the region with the densest LCN (Ca.L/BV $= 0.07\,\mu m\,\mu m^{-3}$) was found in a bone region of the youngest subject (jaw 1, 19 years). However, the local tissue age does not necessarily correspond to the subject age. We speculate that the optimal morphology may be different for different bone conditions (loading, age, mineral homeostasis/demand, species/bone growth rate/time until maturity). To us this underlines that there are general rules for the network architecture, however, at the same time some LCN properties seem to be species-specific. In future studies these differences should be linked to differences in mineral homeostasis between different species to better understand the rules prescribing the network interconnections on the canalicular level. It required to be addressed if and to what extent the mechanical load on the LCN level influences the morphology of the LCN on the canalicular level between neighboring bone cells.

Limitations

Beyond providing new insight into the structure–function relationship of the LCN, the study provides methodological advances for future larger studies and provides 3D masks of the LCN of the nanoCT data together with the morphological analysis free to download so that researchers from the field of computational modeling/biology can utilize these data for more sophisticated analyses. The major limitation of the presented study biologically is a small sample size: for each of six subjects only one pair of lacunae could be included in the analysis, potentially limiting generalizability. However, a nonbiased approach to VOI choice was employed and the overall features that are addressed could be targeted in all patients. The choice of lacunae that have been selected for the analysis was based on the available image quality (i.e., no presence of cracks induced by sample preparation or scanning, and no major image artifacts such as motion artifacts or strong low frequency artifacts due to the local tomography image acquisition and the phase retrieval procedure). Also, the relative positions of the two lacunae and their respective orientations may differ depending on their actual position within the osteon, which has been neglected in this study. Still, our results for all analyzed VOIs are very similar, supporting our assertion that even with all but one connection between two lacunae disrupted, fluid flow within the LCN is maintained though evenly distributed and branched canaliculi. The fluid simulations are simplified, i.e., only a single-phase flow is considered and any cellular dendrites that are present in the canaliculi are ignored, though they clearly impact their surrounding fluid flow. In

addition, it should be noted that nonlinear effects of pore surfaces on the fluid flow may play an important role because the canalicular pores are only few hundreds of nm in diameter and surface–fluid interaction is more crucial than in larger pores. Due to the boundary conditions of the applied fluid models, no assessment about flow into canalicular dead-ends can be made.

4. Conclusion

In the present study, we quantify the interconnections between canaliculi and two corresponding connected osteocyte lacunae. Results show that a large number of individual primary canaliculi are at some point interconnected, thus forming only a few discrete canalicular clusters. The key finding of this article is how the interconnectivity between canaliculi makes the network's transport capabilities and mineral access more robust for the case when individual canaliculi are interrupted. To provide insight into the variability of the reported network properties, our findings are based on the analysis of three different anatomical sites of seven different subjects. In addition, the canalicular architecture of bone tissue of rapidly formed HO is found to be comparable to the LCN of the two other sites.

5. Experimental Section

Samples: Femoral bone, mandibular bone, and HO associated with lower limbs were retrieved from consented human donors ($n = 2$ per condition). The age, sex, and health status of the donors are given in Table 1. Femoral bone samples were acquired for a study approved by the Medical University of Vienna.[47] Ethical approval for mandibular bone was granted by the Ärztekammer Bremen (Studien-Nr. 310). Sample extraction and handling of these samples have previously been reported.[24] HO samples were acquired from consented adult patients undergoing routine excision surgery of HO secondary to major traumatic injuries at University Hospital Birmingham, UK. Tissue transfer and handling were conducted under approval of the National Research Ethics Service (15/NW/0079) and in accordance with the Human Tissue Act 2004. Samples were frozen immediately following surgical removal and stored at $-80\,°C$ until required for sample preparation and analysis. HO samples were thawed, embedded in Tissue-Tek O.C.T. compound (Sakura Finetec USA Inc., Torrance, CA, USA), and sectioned to $100\,\mu m$ thickness using a cryotome. $100 \times 100 \times 4000\,\mu m^3$ batons were subsequently cut manually with a scalpel using an operating microscope. Baton-shaped specimens were then mounted onto aluminum sample holders for imaging.

Data Collection: All synchrotron nanoCT data were collected at the European Synchrotron Radiation Facility (ESRF, Grenoble, France). Measurement of the mandibular and femoral samples was carried out at beamline ID 22NI and experimental details have been previously reported.[24] NanoCT of HO samples was performed at ID 16A of the ESRF under vacuum using a monochromatic focused beam with an energy of 17.05 keV in conjunction with a FReLoN HD E230-84 CCD detector. For each donor 1 sample area of interest was scanned at multiple resolutions to allow an overview followed by a closer inspection of sub volumes of interest. Overview scanning generated 3D images with a voxel size of 120 nm (giving a cylindrical volume of interest (VOI) with diameter and height $245.75\,\mu m$). High-resolution scanning generated 3D images with a voxel size of 50 nm (cylindrical volume of interest diameter and height of $102.40\,\mu m$). Raw image data were collected at four different sample-to-detector distances for each rotation step (32.6, 33.6, 37.6, and 47.6 mm). The focus to detector distance remained constant at 525 mm. Image reconstruction was performed according to previously described protocols.[48] In this imaging setup, the raw collected images are magnified

Fresnel diffraction patterns. To be useable for tomographic imaging, phase retrieval was performed to extract the entangled phase shift and attenuation projections. Retrieved phase maps (2048×2048 pixels) were used as input to a tomographic reconstruction algorithm based on filtered back projection (PyHST, ESRF, Grenoble, Fr). The 3D output images were in the form of a stack of 2048 2D 32-bit floating point grayscale 2048×2048 cross sections. This reconstruction procedure yields a 3D reconstruction of the refractive index decrement, from which the 3D mass density distribution may be ascertained.[48]

Image Processing/Segmentation: Data processing was performed using Fiji, an ImageJ distribution (NIH, Bethesda, MD, USA)[49] and Avizo (Avizo 9.7.0, Thermo Fischer Scientific Inc., Waltham, MA, USA). To reduce noise, a 3D median filter was applied with a neighborhood of $3 \times 3 \times 3$ voxels. Datasets were cropped to subvolumes containing two neighboring lacunae. Subvolumes were randomly selected from regions containing no major artifacts, i.e., avoiding the presence of cracks, delamination, or low-frequency noise (gray value gradients). Where minimal gray value gradient artifacts were present in the images due to the reconstruction process, they were reduced by applying "background correction" in ImageJ followed by a 3D minimum filter with $3 \times 3 \times 3$ voxels to enhance the detection of the canaliculi. Subsequently, a hysteresis thresholding algorithm was used to segment the lacunae and canaliculi from the mineralized bone. The lower threshold was chosen such that seeds were found preferably within all canaliculi. The higher threshold was set to limit the outgrowing into the background (mineralized bone). The quality of the segmentation was then visually inspected in 3D. When necessary, supplemental manual segmentation using multiple tools in Avizo was used to refine the model. The binary dataset contained at least two lacunae and all canaliculi connected to them. Obtaining the final datasets containing two lacunae and only the canaliculi connecting them, representing a single LCN unit cell, required further processing. First, only the masks for the lacunae were extracted by eroding the LCN mask by five voxels followed by a component labeling step. The two largest labels were kept and dilated by ten voxels. One of these masks was then removed from the initially segmented LCN, followed by a connected component labeling. Only the largest region was kept and this procedure was repeated for the second lacuna preserving only the canaliculi between the two lacunae. The accuracy of the boundaries of the computed LCN masks was estimated to not be bigger than ± 1 voxel length.
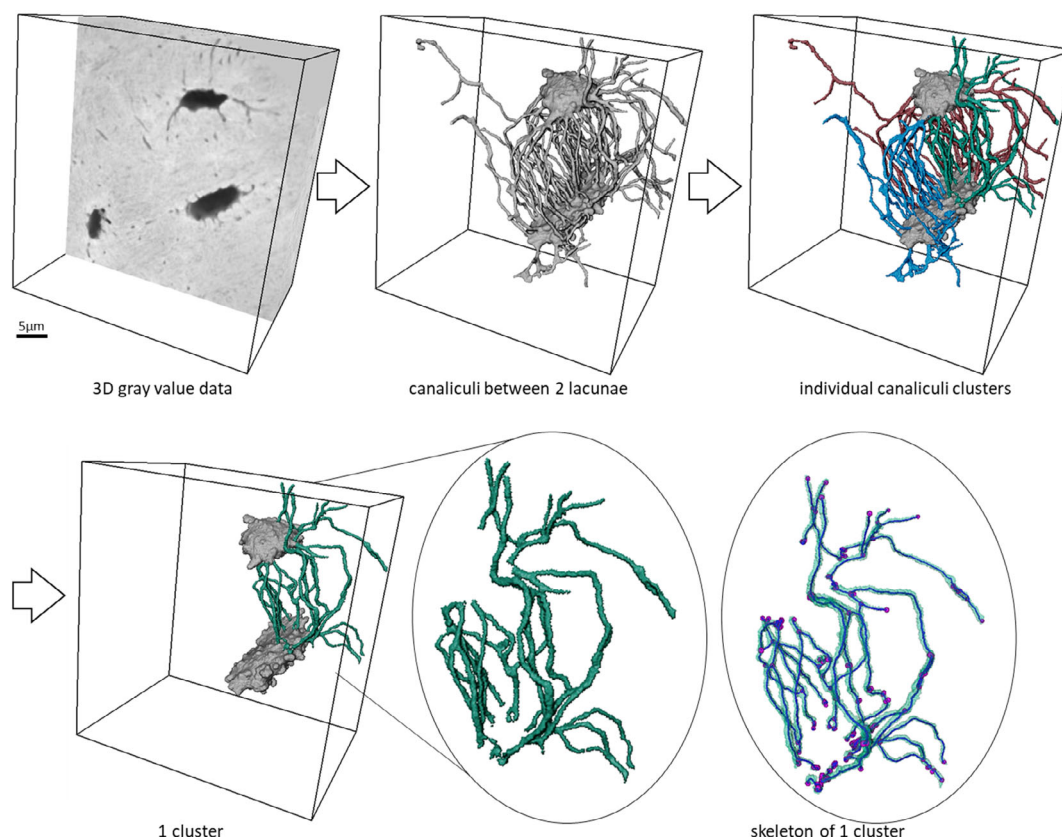
The number of individual canaliculi clusters between two lacunae ($Ca_{clust}.N$) was obtained by removing the lacunae from the dataset and applying a component labeling step. Junctions where three, four, or more canaliculi meet (nodes with order 3, 4, or more, $Ca.Node_{order}$) in the network were counted. The number of nodes per segment (Nodes/Seg) was calculated by dividing the weighted sum of the nodes by the sum of all nodes. To extract the numbers of canaliculi protruding out of one lacuna toward the second ($Ca.N_{LC}$), the difference between a 20-voxel dilated lacuna mask and the original lacuna mask was multiplied with the canaliculi masks. A component labeling step was used to count the number of protruding canaliculi.

The segmented LCN network was morphologically dilated by 200 voxels to obtain a volume containing all the canaliculi that is subsequently defined as the total bone volume (BV.VOI) the network occupies. Further morphological descriptors that were extracted are the canaliculi volume (Ca.V), the canaliculi porosity (Ca.V/BV), and the canaliculi surface area per canalicular volume (Ca.S/Ca.V).

The segmented data were used to evaluate the mineral distributions as a function of the distance to the canaliculi ($Ca.Dist_{50}$, $Ca.Dist_{80}$), as described elsewhere.[3,24]

To further the understanding of the LCN's role in fluid-induced mechanotransduction and material transport (i.e., mineral homeostasis, supply with nutrition), we provide the 3D gray value volumes, the extracted masks of the LCN together with the morphology described in the present study for download, so that it can be further exploited for computational modeling.

Skeletonization: A coordinate system was introduced with the z axis being parallel to the long axis of one of the lacunae and the x axis being

**ADVANCED
SCIENCE NEWS**

www.advancedsciencenews.com

**ADVANCED
NANOBIOMED
RESEARCH**
Open Access

www.advnanobiomedres.com

Figure 6. Workflow showing a 3D gray value data from which two lacunae and the corresponding canaliculi are segmented. Connected canaliculi clusters are shown in one color. One representative cluster is shown to highlight the skeleton extraction. Nodes and junctions are shown in purple and the individual canaliculi segments are shown in pale green.

parallel to its shortest axis. The extracted network was skeletonized with the "autoskeleton" module in Avizo. The skeletons were cleaned by deleting segments smaller than 15 voxels and small loops (defined as single-branch canaliculi that loop back to the lacuna from which they originate). From the skeleton, the total length of all segments between the two lacunae was extracted (Ca.L) and the average canaliculi thickness (Ca.Th) was calculated, assuming a circular shape and using the Ca.V. An average segment length (Ca.L$_{seg}$) was estimated in Equation (1) as

$$Ca.L_{seg} = \frac{2Ca.L}{\left(\sum Ca.N_{LC} + 3Ca.Node_3 + 4Ca.Node_4 + 5Ca.Node_{junction}\right)} \quad (1)$$

The spatial orientation of each segment with respect to the lacuna long axis was computed and given by the angle theta which ranges between 0° and 90°. The angles were normalized by the volume of the segment. The anisotropy of the canalicular networks (LoA) was quantified as follows: the histograms, composed of ten bins of theta, were computed and the variance of the resulting bin heights was computed. The LoA is lower for a more homogeneous angular distribution, represented by a smaller variance of the bins in the histogram of theta. A schematic of the full image analysis workflow is given in **Figure 6**.

Fluid Simulation: One segmented dataset per bone type (jaw 1, femur 1, HO 1) was additionally used for fluid analyses in Thermo Scientific Avizo Software (Version 2020.2, Thermo Fischer Scientific Inc., Waltham, MA, USA) using the XLab toolbox. A surface determination was applied on the binary data using the isovalue approach. The parallel planes defining the fluid inflow and outflow were chosen within the lacunae. Transport phenomena simulations were performed in the experiment mode, analyzing the stationary field (e.g., velocity) of a laminar flow of an incompressible medium for both directions. The simulations were stopped when the estimation of the convergence criterion at each iteration reached 10^{-5} or the number of iterations reached 10^6. To simulate a compromised LCN, the datasets were further manipulated so that all canaliculi except one were virtually cut close to one lacuna. The fluid analyses were then repeated for both flow directions. Absolute permeability is defined as the measure of the ability of a porous material to transmit a single-phase liquid in units of darcy (d), with $1d = 0.987\,\mu m^2$. Through Darcy's law the fluid and flow were computed. To numerically estimate the absolute permeability, the Strokes equations are solved. All simulation were performed using the XLab toolbox of Avizo.

Supporting Information

Supporting Information is available from the Wiley Online Library or from the author.

Acknowledgements

Open Access funding enabled and organized by Projekt DEAL. [Correction added on April 8, 2022, after first online publication: Projekt DEAL funding statement has been added.]

Conflict of Interest

The authors declare no conflict of interest.

Data Availability Statement

The data that support the findings of this study are available from the corresponding author upon reasonable request.

Keywords

bone mineral homeostasis, canalicular network, osteocyte lacunar networks, synchrotron nano computed tomography

[1] H. Qing, L. Ardeshirpour, P. D. Pajevic, V. Dusevich, K. Jähn, S. Kato, J. Wysolmerski, L. F. Bonewald, *J. Bone Miner. Res.* **2012**, *27*, 1018.

[2] B. Hesse, M. Langer, P. Varga, A. Pacureanu, P. Dong, S. Schrof, N. Männicke, H. Suhonen, C. Olivier, P. Maurer, G. J. Kazakia, K. Raum, F. Peyrin, D. Heymann, *PLoS One* **2014**, *9*, e88481.

[3] P. Dong, S. Haupert, B. Hesse, M. Langer, P.-J. Gouttenoire, V. Bousson, F. Peyrin, *Bone* **2014**, *60*, 172.

[4] Y. Carter, C. D. L. Thomas, J. G. Clement, D. M. L. Cooper, *J. Struct. Biol.* **2013**, *183*, 519.

[5] A. M. Ashique, L. S. Hart, C. D. L. Thomas, J. G. Clement, P. Pivonka, Y. Carter, D. D. Mousseau, D. M. L. Cooper, *Bone Rep.* **2017**, *7*, 9.

[6] L. F. Bonewald, *J. Musculoskelet. Neuronal Interact.* 5, 321.

[7] B. Yu, A. Pacureanu, C. Olivier, P. Cloetens, F. Peyrin, *Sci. Rep.* **2020**, *10*, 1.

[8] P. Dong, A. Pacureanu, M. A. Zuluaga, C. Olivier, Q. Grimal, F. Peyrin, *Image Anal. Stereol.* **2014**, *33*, 1.

[9] T. Beno, Y. J. Yoon, S. C. Cowin, S. P. Fritton, *J. Biomech.* **2006**, *39*, 2378.

[10] L. Cardoso, S. P. Fritton, G. Gailani, M. Benalla, S. C. Cowin, *J. Biomech.* **2013**, *46*, 253.

[11] R. Weinkamer, P. Kollmannsberger, P. Fratzl, *Curr. Osteoporos. Rep.* **2019**, *17*, 186.

[12] D. Sharma, C. Ciani, P. A. R. Marin, J. D. Levy, S. B. Doty, S. P. Fritton, *Bone* **2012**, *51*, 488.

[13] A. Roschger, P. Roschger, W. Wagermaier, J. Chen, A. F. Tolvan, F. Repp, S. Blouin, A. Berzlanovich, G. M. Gruber, K. Klaushofer, P. Fratzl, R. Weinkamer, *Bone* **2019**, *123*, 76.

[14] P. Varga, B. Hesse, M. Langer, S. Schrof, N. Männicke, H. Suhonen, A. Pacureanu, D. Pahr, F. Peyrin, K. Raum, *Biomech. Model. Mechanobiol.* **2015**, *14*, 267.

[15] N. K. Wittig, M. Laugesen, M. E. Birkbak, F. L. GansmoBach-, A. Pacureanu, S. Bruns, M. H. Wendelboe, A. Brüel, H. O. Sørensen, J. S. Thomsen, H. Birkedal, *ACS Nano* **2019**, *13*, 6421.

[16] M. Kerschnitzki, P. Kollmannsberger, M. Burghammer, G. N. Duda, R. Weinkamer, W. Wagermaier, P. Fratzl, *J. Bone Miner. Res.* **2013**, *28*, 1837.

[17] S. L. Dallas, D. S. Moore, *Bone* **2020**, *138*, 115463.

[18] A. F. TolVan, V. Schemenz, W. Wagermaier, A. Roschger, H. Razi, I. Vitienes, P. Fratzl, B. M. Willie, R. Weinkamer, *Proc. Natl. Acad. Sci.* **2020**, *117*, 32251.

[19] A. F. Tolvan, A. Roschger, F. Repp, J. Chen, P. Roschger, A. Berzlanovich, G. M. Gruber, P. Fratzl, R. Weinkamer, A. F. VanTol Tolvan, *Biomech. Model. Mechanobiol.* **2020**, *19*, 823.

[20] S. L. Dallas, M. Prideaux, L. F. Bonewald, *Endocr. Rev.* **2013**, *34*, 658.

[21] S.-J. Estermann, S. Scheiner, *Front. Phys.* **2018**, *6*, 76.

[22] S. W. Verbruggen, T. J. Vaughan, L. M. McNamara, *Biomech. Model. Mechanobiol.* **2014**, *13*, 85.

[23] S. Mishra, M. L. TateKnothe, *Anat. Rec.* **2003**, *273A*, 752.

[24] B. Hesse, P. Varga, M. Langer, A. Pacureanu, S. Schrof, N. Männicke, H. Suhonen, P. Maurer, P. Cloetens, F. Peyrin, K. Raum, *J. Bone Miner. Res.* **2015**, *30*, 346.

[25] D. Ruffoni, P. Fratzl, P. Roschger, K. Klaushofer, R. Weinkamer, *Bone* **2007**, *40*, 1308.

[26] H. Qing, L. F. Bonewald, *Int. J. Oral Sci.* **2009**, *1*, 59.

[27] P. Kollmannsberger, M. Kerschnitzki, F. Repp, W. Wagermaier, R. Weinkamer, P. Fratzl, *New J. Phys.* **2017**, *19*, 073019.

[28] P. Varga, A. Pacureanu, M. Langer, H. Suhonen, B. Hesse, Q. Grimal, P. Cloetens, K. Raum, F. Peyrin, *Acta Biomater.* **2013**, *9*, 8118.

[29] V. Ebacher, P. Guy, T. R. Oxland, R. Wang, *Acta Biomater.* **2012**, *8*, 1093.

[30] S. Qiu, D. S. Rao, D. P. Fyhrie, S. Palnitkar, A. M. Parfitt, *Bone* **2005**, *37*, 10.

[31] D. B. Burr, R. B. Martin, M. B. Schaffler, E. L. Radin, *J. Biomech.* **1985**, *18*, 189.

[32] B. Hesse, N. Männicke, A. Pacureanu, P. Varga, M. Langer, P. Maurer, F. Peyrin, K. Raum, *J. Microsc.* **2014**, *255*, 158.

[33] T. Rolvien, F. N. Schmidt, P. Milovanovic, K. Jähn, C. Riedel, S. Butscheidt, K. Püschel, A. Jeschke, M. Amling, B. Busse, *Sci. Rep.* **2018**, *8*, 1.

[34] P. Milovanovic, E. A. Zimmermann, A. Scheidt vom, B. Hoffmann, G. Sarau, T. Yorgan, M. Schweizer, M. Amling, S. Christiansen, B. Busse, *Small* **2017**, *13*, 1602215.

[35] P. Milovanovic, B. Busse, *Curr. Osteoporos. Reports* **2019**, *17*, 105.

[36] L. A. M. -LewisTiede, S. L. Dallas, *Bone* **2019**, *122*, 101.

[37] L. M. -LewisTiede, Y. Xie, M. A. Hulbert, R. Campos, M. R. Dallas, V. Dusevich, L. F. Bonewald, S. L. Dallas, *Aging* **2017**, *9*, 2190.

[38] P. Milovanovic, E. A. Zimmermann, M. Hahn, D. Djonic, K. Püschel, M. Djuric, M. Amling, B. Busse, *ACS Nano* **2013**, *7*, 7542.

[39] A. Iordachescu, H. D. Amin, S. M. Rankin, R. L. Williams, C. Yapp, A. Bannerman, A. Pacureanu, O. Addison, P. A. Hulley, L. M. Grover, *Adv. Biosyst.* **2018**, *2*, 1700156.

[40] V. Gatti, E. M. Azoulay, S. P. Fritton, *J. Biomech.* **2018**, *66*, 127.

[41] M. Langer, A. Pacureanu, H. Suhonen, Q. Grimal, P. Cloetens, F. Peyrin, *PLoS One* **2012**, *7*, e35691.

[42] A. Ciani, H. Toumi, S. Pallu, E. H. R. Tsai, A. Diaz, M. Guizar-Sicairos, M. Holler, E. Lespessailles, C. M. Kewish, *Bone Rep.* **2018**, *9*, 122.

[43] S. P. Fritton, S. Weinbaum, *Annu. Rev. Fluid Mech.* **2008**, *41*, 347.

[44] Y. Wang, L. M. McNamara, M. B. Schaffler, S. Weinbaum, *Proc. Natl. Acad. Sci.* **2007**, *104*, 15941.

[45] Y. Han, S. C. Cowin, M. B. Schaffler, S. Weinbaum, *Proc. Natl. Acad. Sci.* **2004**, *101*, 16689.

[46] F. Repp, P. Kollmannsberger, A. Roschger, M. Kerschnitzki, A. Berzlanovich, G. Gruber, P. Roschger, W. Wagermaier, R. Weinkamer, *Bone Rep.* **2017**, *6*, 101.

[47] E. Dall'Ara, B. Luisier, R. Schmidt, F. Kainberger, P. Zysset, D. Pahr, *Bone* **2013**, *52*, 27.

[48] B. Yu, A. Weber, A. Pacureanu, M. Langer, C. Olivier, P. Cloetens, F. Peyrin, *Opt. Express* **2018**, *26*, 11110.

[49] J. Schindelin, I. Carreras-Arganda, E. Frise, V. Kaynig, M. Longair, T. Pietzsch, S. Preibisch, C. Rueden, S. Saalfeld, B. Schmid, J.-Y. Tinevez, D. J. White, V. Hartenstein, K. Eliceiri, P. Tomancak, A. Cardona, *Nat. Methods* **2012**, *9*, 676.